Effects of higher order propagation modes in vocal tract like geometries

Rémi Blandin[a)]
GIPSA-Lab, Unité Mixte de Recherche au Centre National de la Recherche Scientifique 5216, Grenoble Campus, St Martin dHeres, F-38402, France

Marc Arnela
Grup de recerca en Tecnologies Mèdia, La Salle, Universitat Ramon Llull C/Quatre Camins 2, E-08022 Barcelona, Catalonia, Spain

Rafael Laboissière
PACS Team, INSERM Unit 1028: Cognition and Brain Dynamics, Lyon Neurosciences Research Centre, EPU-ISTIL, Claude Bernard University, Boulevard du 11 Novembre 1918, 69622 Villeurbanne, France

Xavier Pelorson
GIPSA-Lab, Unité Mixte de Recherche au Centre National de la Recherche Scientifique 5216, Grenoble Campus, St Martin dHeres, F-38402, France

Oriol Guasch
Grup de recerca en Tecnologies Mèdia, La Salle, Universitat Ramon Llull C/Quatre Camins 2, E-08022 Barcelona, Catalonia, Spain

Annemie Van Hirtum and Xavier Laval
GIPSA-Lab, Unité Mixte de Recherche au Centre National de la Recherche Scientifique 5216, Grenoble Campus, St Martin dHeres, F-38402, France

(Received 4 September 2014; revised 20 November 2014; accepted 17 December 2014)

In this paper, a multimodal theory accounting for higher order acoustical propagation modes is presented as an extension to the classical plane wave theory. This theoretical development is validated against experiments on vocal tract replicas, obtained using a 3D printer and finite element simulations. Simplified vocal tract geometries of increasing complexity are used to investigate the influence of some geometrical parameters on the acoustical properties of the vocal tract. It is shown that the higher order modes can produce additional resonances and anti-resonances and can also strongly affect the radiated sound. These effects appear to be dependent on the eccentricity and the cross-sectional shape of the geometries. Finally, the comparison between the simulations and the experiments points out the importance of taking visco-thermal losses into account to increase the accuracy of the resonance bandwidths prediction. © *2015 Acoustical Society of America*.
[http://dx.doi.org/10.1121/1.4906166]

[ZZ] Pages: 832–843

I. INTRODUCTION

In voice production, as well as in voice analysis, such as inverse filtering, for instance, plane wave propagation is assumed inside the vocal tract. In other words, it is assumed that the acoustic pressure only depends on the propagation direction and that a one-dimensional description of the vocal tract shape, using an area function, is sufficient to predict the acoustic field both inside and outside of the vocal tract. Classical textbooks (e.g., Fant, 1971; Flanagan, 1972; Stevens, 2000; O'Shaughnessy, 1987) often indicate that these descriptions rely on a low frequency assumption, so the limits of validity of the underlying theory are not clearly established.

As our knowledge concerning the sound sources increases (e.g., Kniesburges, 2013; Zheng *et al.*, 2011; Jackson and Shadle, 2000; Thomson *et al.*, 2005), the ability to extract the three dimensional vocal tract geometry also increases (e.g., Story, 2008; Narayanan *et al.*, 1995; Woo *et al.*, 2012). *In vivo* measurements, or computer simulations, often enhance spectacular departures from plane wave theory even at moderate frequencies (on the order of 5 kHz, Dang and Honda, 1997; El-Masri *et al.*, 1998; Arnela and Guasch, 2013; Takemoto *et al.*, 2010; Vampola *et al.*, 2013).

As a plausible explanation for these departures, we first present a theoretical investigation of sound propagation inside a simplified vocal-tract-like waveguide focusing, in particular, upon the three dimensional effects due to the presence of higher order acoustical modes. The goal of this paper is not only to apply a theoretical model to account for them but also to compare the predictions with experiments and specific observations relating the vocal-tract-like geometries.

The validation of the implementation of the proposed theoretical model will be performed against finite element numerical simulations and the acoustic measurements performed on mechanical replicas of the vocal tract.

[b)]Author to whom correspondence should be addressed. Electronic mail: remi.blandin@gipsa-lab.grenoble-inp.fr

We will consider geometries with increasing degrees of complexity. Simple academic approximations, such as two-tube concatenations, will also be useful to enhance some three dimensional geometrical effects.

The paper is structured as follows. The multimodal theory is detailed in Sec. II. The geometries used for this study, the experimental setup, the transfer function measurement method, and the finite element simulation method are presented in Sec. III. In Sec. IV, the measurement and simulation results are compared and the difference between the geometries are discussed.

II. MULTIMODAL THEORY

In this section, the multimodal theory used to compute the acoustic pressure and velocity in a variable cross-section waveguide is detailed. This theory has been developed by several authors including Roure (1976), Kergomard *et al.* (1989), Pagneux *et al.* (1996), and Kemp (2002). It has already been applied to the vocal tract case with rectangular cross-sections by Motoki *et al.* (2000). The aforementioned works are extended to consider straight vocal tract geometries with arbitrary cross-sections and eccentric junctions. The strategy is to divide the waveguide in a succession of constant cross-section waveguides in which the Helmholtz equation can easily be solved. By applying the continuity equations of the pressure and the velocity at each junction and taking into account the radiation impedance at the open end of the waveguide, one can back-propagate the impedance or admittance matrices from the open end to the entrance. The acoustic pressure and velocity can then be propagated from the entrance toward the exit and computed in each section.

In what follows the assumptions of linear acoustics (small perturbations assumption) are considered.

A. Constant cross-section waveguides

The pressure p and the velocity v_{x_3} in the propagation direction x_3 inside a waveguide with arbitrary constant cross-section shape can be expressed as the summation of the contribution of an infinity of propagation modes ψ_n (Morse and Ingard, 1986) weighted by a propagation factor $(A_n e^{-jk_n x_3} \pm B_n e^{jk_n x_3})$ and a time evolution factor $e^{j\omega t}$,

$$\begin{cases} p = \sum_{n=0}^{\infty} \psi_n(x_1,x_2)\left(A_n e^{-jk_n x_3} + B_n e^{jk_n x_3}\right) e^{j\omega t}, \\ v_{x_3} = \dfrac{1}{\omega\rho}\sum_{n=0}^{\infty} k_n \psi_n(x_1,x_2)\left(A_n e^{-jk_n x_3} - B_n e^{jk_n x_3}\right) e^{j\omega t}, \end{cases} \tag{1}$$

where (x_1, x_2, x_3) is a generalized coordinate system, x_3 is the propagation direction, ω is the angular frequency, and ρ is the constant air density. The functions ψ_n are the solutions of the two dimensional Helmholtz equation for the cross-section shape. They are part of an orthogonal modal basis and they satisfy a normalization condition

$$\int_S \psi_m^* \psi_n dS = S\delta_{mn}, \tag{2}$$

where S is the cross-section surface.

For rectangular cross-sections ψ_n are a combination of sine and cosine functions, for circular cross-sections they are a combination of Bessel, sine and cosine functions and for elliptical cross-sections they are a combination of Mathieu (Abramowitz and Stegun, 1972), sine and cosine functions. In the general case there is no analytical expression for ψ_n. It is, however, possible to get an approximation for them using numerical methods such as finite differences or finite elements.

To each mode ψ_n of this basis corresponds a modal wavenumber k_n in the propagation direction x_3 which satisfies the dispersion relationship

$$k^2 = k_{x_1}^2 + k_{x_2}^2 + k_n^2, \tag{3}$$

where $k = w/c$ is the free field wavenumber and c is the sound speed at rest.

To avoid heavy expressions it is more convenient to use a vector notation (throughout this article vectors and matrix are in bold) and to omit the $e^{j\omega t}$ factor:

$$\begin{cases} p = \boldsymbol{\psi}^t \mathbf{P}, \\ v_{x_3} = \dfrac{1}{S}\boldsymbol{\psi}^t \mathbf{U}, \end{cases} \tag{4}$$

where superscript t is the transpose operator, $\boldsymbol{\psi} = [\psi_1(x_1, x_2), \psi_2(x_1,x_2), \ldots, \psi_n(x_1,x_2)]^t$, $\mathbf{P} = [A_1 e^{-jk_1x_3} + B_1 e^{jk_1x_3}, A_2 e^{-jk_2x_3} + B_2 e^{jk_2x_3}, \ldots, A_n e^{-jk_nx_3} + B_n e^{jk_nx_3}]^t$, and $\mathbf{U} = [k_1 S/\omega\rho(A_1 e^{-jk_1x_3} - B_1 e^{jk_1x_3}), k_2 S/\omega\rho(A_2 e^{-jk_2x_3} - B_2 e^{jk_2x_3}), \ldots, k_n S/\omega\rho(A_n e^{-jk_nx_3} - B_n e^{jk_nx_3})]^t$.

Solving the wave equation with the expressions of Eq. (4) for the pressure and the velocity allows writing two relationships between the pressure and velocity modal amplitudes $\mathbf{P}$ and $\mathbf{U}$ at two different locations. Consider two points located within the waveguide at the abscissas $x_3^{(0)}$ and $x_3^{(1)}$. $\mathbf{P}^{(0)}$ and $\mathbf{U}^{(0)}$ at $x_3^{(0)}$ can be known from $\mathbf{P}^{(1)}$ and $\mathbf{U}^{(1)}$ at $x_3^{(1)}$ with

$$\mathbf{P}^{(0)} = \mathbf{D_1}\mathbf{P}^{(1)} + \mathbf{D_2}\mathbf{Z}_c\mathbf{U}^{(1)}, \tag{5}$$

$$\mathbf{U}^{(0)} = \mathbf{D_2}\mathbf{Z}_c^{-1}\mathbf{P}^{(1)} + \mathbf{D_1}\mathbf{U}^{(1)}, \tag{6}$$

where $\mathbf{D}_1 = \mathrm{diag}(\cos(k_n d))$ is a diagonal matrix whose terms are $\cos(k_n d)$ with $d = x_3^{(1)} - x_3^{(0)}$, $\mathbf{D}_2 = \mathrm{diag}(j\sin(k_n d))$, and $\mathbf{Z}_c$ is the characteristic impedance matrix obtained as $\mathbf{Z}_c = \mathrm{diag}(k\rho c/k_n S)$.

Using $\mathbf{P}^{(i)} = \mathbf{Z}^{(i)}\mathbf{U}^{(i)}$, with $i = 0$ or $i = 1$, allows writing a relationship between the impedance matrices $\mathbf{Z}^{(0)}$ and $\mathbf{Z}^{(1)}$ at $x_3^{(0)}$ and $x_3^{(1)}$,

$$\mathbf{Z}^{(0)} = [\mathbf{D_1}\mathbf{Z}^{(1)} + \mathbf{D_2}\mathbf{Z}_c]\,[\mathbf{D_2}\mathbf{Z}_c^{-1}\mathbf{Z}^{(1)} + \mathbf{D_1}]^{-1}. \tag{7}$$

Following the same procedure and using the equation $\mathbf{U}^{(i)} = \mathbf{Y}^{(i)}\mathbf{P}^{(i)}$ allows us to write three other relationships between the impedance and the admittance matrices at $x_3^{(0)}$ and $x_3^{(1)}$,

$$\mathbf{Z}^{(0)} = [\mathbf{D_1} + \mathbf{D_2}\mathbf{Z}_c\mathbf{Y}^{(1)}]\,[\mathbf{D_2}\mathbf{Z}_c^{-1} + \mathbf{D_1}\mathbf{Y}^{(1)}]^{-1}, \tag{8}$$

$$\mathbf{Y}^{(0)} = [\mathbf{D_1}\mathbf{Y}^{(1)} + \mathbf{D_2}\mathbf{Z}_c^{-1}]\,[\mathbf{D_2}\mathbf{Z}_c\mathbf{Y}^{(1)} + \mathbf{D_1}]^{-1}, \tag{9}$$

$$\mathbf{Y}^{(0)} = [\mathbf{D_1} + \mathbf{D_2}\mathbf{Z}_c^{-1}\mathbf{Z}^{(1)}]\,[\mathbf{D_2}\mathbf{Z}_c + \mathbf{D_1}\mathbf{Z}^{(1)}]^{-1}. \tag{10}$$

B. Junctions between sections

At a junction between two ducts with different cross-sections it is necessary to find a relationship between the modal basis of each section. Let us consider two ducts a and b whose cross-sectional surfaces are S_a and S_b, respectively (see Fig. 1). Applying the continuity of both the pressure and the velocity on each side of the junction yields

$$\boldsymbol{\psi}_a^t\mathbf{P}_a = \boldsymbol{\psi}_b^t\mathbf{P}_b, \tag{11}$$

$$\frac{1}{S_a}\boldsymbol{\psi}_a^t\mathbf{U}_a = \frac{1}{S_b}\boldsymbol{\psi}_b^t\mathbf{U}_b. \tag{12}$$

Hereafter the subscript b always refers to the duct with the largest cross-section and the subscript a to the smallest one. If one assumes that $S_a < S_b$ and S_a lies inside S_b, multiplying both sides of Eq. (11) with $\boldsymbol{\psi}_a^*/S_a$ and integrating over S_a leads to

$$\mathbf{P}_a = \frac{1}{S_a}\left[\int_{S_a}\boldsymbol{\psi}_a^*\boldsymbol{\psi}_b^t dS_a\right]\mathbf{P}_b. \tag{13}$$

In the same way multiplying Eq. (12) with $\boldsymbol{\psi}_b^*$ and integrating over S_b yields

$$\mathbf{U}_b = \frac{1}{S_a}\left[\int_{S_b}\boldsymbol{\psi}_b^*\boldsymbol{\psi}_a^t dS_b\right]\mathbf{U}_a. \tag{14}$$

Yet we have $\boldsymbol{\psi}_a = 0$ on $S_b - S_a$, so

$$\int_{S_b}\boldsymbol{\psi}_b^*\boldsymbol{\psi}_a^t dS_b = \int_{S_a}\boldsymbol{\psi}_b^*\boldsymbol{\psi}_a^t dS_a = \left[\int_{S_a}\boldsymbol{\psi}_a^*\boldsymbol{\psi}_b^t dS_a\right]^\dagger,$$

where the dagger represents the transpose conjugate. Thus defining $\mathbf{F}$ as

$$\mathbf{F} = \frac{1}{S_a}\int_{S_a}\boldsymbol{\psi}_a^*\boldsymbol{\psi}_b^t dS. \tag{15}$$

Equations (13) and (14) can be rewritten as

$$\mathbf{P}_a = \mathbf{F}\mathbf{P}_b, \tag{16}$$

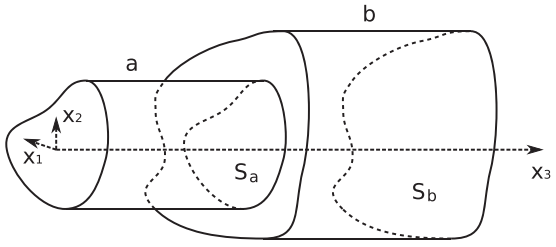

FIG. 1. Junction between two ducts of arbitrary cross-section shape.

$$\mathbf{U}_b = \mathbf{F}^\dagger\mathbf{U}_a. \tag{17}$$

Given that $\mathbf{P} = \mathbf{Z}\mathbf{U}$ and $\mathbf{U} = \mathbf{Y}\mathbf{P}$, Eqs. (16) and (17) can be expressed as

$$\mathbf{Z}_a = \mathbf{F}\,\mathbf{Z}_b\mathbf{F}^\dagger, \tag{18}$$

$$\mathbf{Y}_b = \mathbf{F}^\dagger\mathbf{Y}_a\mathbf{F}. \tag{19}$$

C. Computation of the acoustic pressure and velocity fields

The radiation impedance matrix at the open end (last cross-section) can be obtained analytically in the case of a circular or a rectangular waveguide flanged into an infinite baffle using Zorumski (1973) and Kemp *et al.* (2001) expressions, while for an arbitrary shaped cross-section this can be achieved by numerically integrating the expression

$$Z_{mn} = \frac{j\omega\rho}{2\pi S^2}\int_S dS\int_S \psi_m(x'_1, x'_2)\psi_n(x_1, x_2)\frac{e^{-jkh}}{h}dS, \tag{20}$$

with $h = \sqrt{(x_1 - x'_1)^2 + (x_2 - x'_2)^2}$ and S being the cross-section surface at the open end of the waveguide. This impedance matrix can be back-propagated towards the entrance of the waveguide. To do so, Eqs. (18) and (19) allow one to propagate the impedance and admittance matrices through a junction. However, these matrices can be poorly conditioned and inversion must be avoided. Thus the impedance matrix must be used for expansions and the admittance matrix for contractions. This constraint introduces four different cases for the projection of the impedance or admittance matrices from a junction to another which are described in Fig. 2.

For case (a), both junctions are expanding so the impedance matrices can be propagated through the junctions with Eq. (18) and $\mathbf{Z}^{(0)}$ can be computed from $\mathbf{Z}^{(1)}$ with Eq. (7). On the contrary, in case (c) both junctions are contracting so the admittance matrices can be propagated through the junctions with Eq. (19) and $\mathbf{Y}^{(0)}$ can be computed from $\mathbf{Y}^{(1)}$ with Eq. (9). Case (b) is expanding and then contracting, so the admittance matrix can be propagated through the junction of

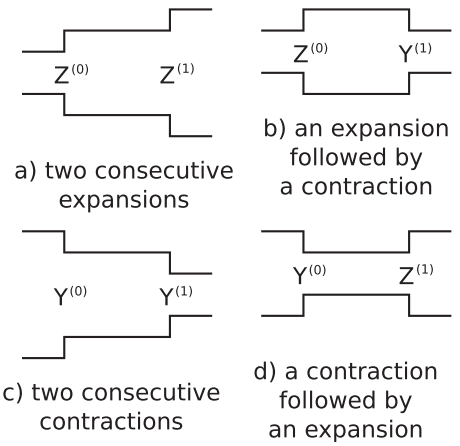

FIG. 2. The four different configurations for backward projection of impedance and admittance matrices.

the right and the impedance matrix can be propagated through the junction of the left. The impedance $\mathbf{Z}^{(0)}$ can be computed from the admittance $\mathbf{Y}^{(1)}$ with Eq. (8). The opposite case (d) is contracting and then expanding, so the impedance matrix can be propagated through the junction of the right and the admittance matrix can be propagated through the junction of the left. The admittance $\mathbf{Y}^{(0)}$ can be computed from the impedance $\mathbf{Z}^{(1)}$ with Eq. (10).

However $\mathbf{D_1}$ and $\mathbf{D_2}$ in Eqs. (7)–(10) contain very large terms for evanescent modes which induce round off numerical errors. To ensure numerical stability, a new diagonal matrix $\mathbf{D_3} = \mathrm{diag}(\tan(k_n d))$ is introduced. Equations (7)–(10) are rewritten using only $\mathbf{D_3}^{-1}$ and $\mathbf{D_2}^{-1}$ instead of $\mathbf{D_1}$ and $\mathbf{D_2}$,

$$\mathbf{Z}^{(0)} = (j\mathbf{D_3})^{-1}\mathbf{Z}_c - \mathbf{D_2}^{-1}\mathbf{Z}_c[\mathbf{Z}^{(1)} + (j\mathbf{D_3})^{-1}\mathbf{Z}_c]\mathbf{D_2}^{-1}\mathbf{Z}_c, \tag{21}$$

$$\mathbf{Z}^{(0)} = (j\mathbf{D_3})^{-1}\mathbf{Z}_c - \mathbf{D_2}^{-1}\mathbf{Z}_c[\mathbf{I} + (j\mathbf{D_3})^{-1}\mathbf{Y}^{(1)}\mathbf{Z}_c]\mathbf{D_2}^{-1}\mathbf{Z}_c, \tag{22}$$

$$\mathbf{Y}^{(0)} = (j\mathbf{D_3})^{-1}\mathbf{Z}_c^{-1} - \mathbf{D_2}^{-1}\mathbf{Z}_c^{-1}[\mathbf{Y}^{(1)} + (j\mathbf{D_3})^{-1}]\mathbf{D_2}^{-1}\mathbf{Z}_c^{-1}, \tag{23}$$

$$\mathbf{Y}^{(0)} = (j\mathbf{D_3})^{-1}\mathbf{Z}_c^{-1} - \mathbf{D_2}^{-1}\mathbf{Z}_c^{-1} \times [\mathbf{I} + (j\mathbf{D_3})^{-1}\mathbf{Z}_c^{-1}\mathbf{Z}^{(1)}]\mathbf{D_2}^{-1}\mathbf{Z}_c^{-1}. \tag{24}$$

In the case of a source located at the entrance, the pressure or the acoustic velocity of the source can be projected on the modal basis which describes the pressure and velocity field at the source location. For a source delivering a velocity v_s on a surface S_s, the modal amplitude $\mathbf{U}_s$ corresponding to the source can be found with

$$\mathbf{U}_s = \int_{S_s} \boldsymbol{\psi} * v_s dS_s. \tag{25}$$

The pressure and the velocity modal amplitudes can be then propagated from the entrance to the open end. Introducing $\mathbf{Y}^{(1)}$ and $\mathbf{Z}^{(1)}$ into Eqs. (5) and (6) leads to

$$\mathbf{P}^{(1)} = [\mathbf{D_1} + \mathbf{D_2}\mathbf{Z}_c\mathbf{Y}^{(1)}]^{-1}\mathbf{P}^{(0)}, \tag{26}$$

$$\mathbf{U}^{(1)} = [\mathbf{D_2}\mathbf{Z}_c^{-1}\mathbf{Z}^{(1)} + \mathbf{D_1}]^{-1}\mathbf{U}^{(0)}, \tag{27}$$

which allow one to propagate $\mathbf{P}$ or $\mathbf{U}$ (depending on whether the impedance or the admittance is known) through a constant cross-section waveguide portion. The vectors $\mathbf{P}$ and $\mathbf{U}$ can then be propagated through the junctions using Eqs. (16) and (17). Equations (5) and (6) allow to compute $\mathbf{P}$ and $\mathbf{U}$ at any abscissa x_3 and the pressure p and the axial velocity v_{x_3} can be computed with Eq. (1) at any point inside the waveguide.

The pressure field radiated by the waveguide can be computed using the Rayleigh–Sommerfield integral

$$p(x_1, x_2, x_3) = \sum_{n=0}^{\infty} \frac{j\omega\rho}{2\pi S} \int_{S'} U_n \psi_n(x'_1, x'_2) \frac{e^{jkh}}{h} dS', \tag{28}$$

with $h = \sqrt{(x_1 - x'_1)^2 + (x_2 - x'_2)^2 + (x_3 - x'_3)^2}$, S' being the surface at the open end of the waveguide and $(x'_1,\ x'_2,\ x'_3)$ the coordinates of the points on S'.

This multimodal theory has been implemented with OCTAVE to perform simulations. Finite differences have been used to compute the ψ_n functions. This simulation method will be called the multimodal method (MM) hereafter.

III. METHODS

A. Vocal tract geometries

Five different vocal tract geometries are considered in this work (see Fig. 3).

First, in order to study the effect of the eccentricity of a junction between two waveguide sections, two geometries have been considered.

(1) One with two cylindrical tubes sharing the same central axis [Fig. 3(a), called the "centric case" hereafter].
(2) One with two cylindrical tubes sharing a common line on the edge [Fig. 3(b), called the "eccentric case" hereafter].

The two tubes of both geometries are 85 mm long and have an internal diameter of 14.5 mm and 29.5 mm. Although these geometries are a very rough two tube approximation of the vocal tract, they can be seen as a vowel /a/ reproduction (Fant, 1971). Two replicas of these geometries have been built with Plexiglas tubes to perform measurements.

Three more realistic vocal tract geometries of vowel /a/ have then been considered using a vocal tract area function provided by Story (2008). Each of these three simplified vocal tracts is designed to investigate a geometrical detail effect.

(1) One has circular cross-sections sharing the same central axis [Fig. 3(c), called "centric /a/" hereafter].
(2) One has circular cross-sections sharing a common line on the edge [Fig. 3(d), called "eccentric /a/" hereafter].
(3) One has elliptical cross-sections sharing a common line on the edge [Fig. 3(e), called "elliptic /a/" hereafter].

In the case of the eccentric and the elliptical /a/ cases, the length of each section has been adjusted so that the total length of the line that connects the centers of each cross-section (called the midline hereafter) is the same as for centric /a/. Otherwise, numerical tests have shown that a non-expected shift down of the formant positions can be produced (up to about 2%). Thus the length of each section is 3.88, 3.82, and 3.86 mm for the centric, eccentric, and elliptic /a/, respectively. On the other hand, the eccentricity of the mouth aperture, obtained from Fromkin (1964) for vowel /a/, has been applied to all cross-sections to generate the elliptical vocal tract, as done in Arnela *et al.* (2013).

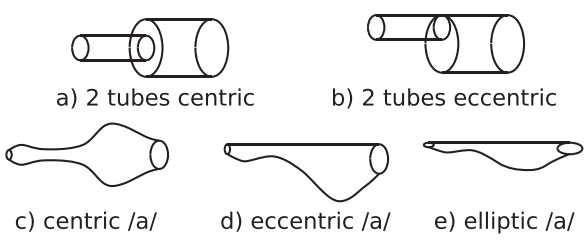

FIG. 3. Vocal tract geometries used for the experiments and simulations.

Three replicas of these geometries have been built using a 3D printer (ProJet 3510 SD).

B. Experimental setup

An experimental setup inspired from the work of Motoki *et al.* (1992) has been developed to measure the acoustic pressure inside and outside of the vocal tract replicas. A scheme of this setup is presented in Fig. 4. In order to be able to generate sound over the frequency range relevant in speech (100 to 10 000 Hz), two different acoustic sources have been needed. Because a loudspeaker would not provide enough acoustic energy, compression chambers have become necessary. Two chambers have been used: a Monacor KU-916T and an Eminence PSD:2002S-8 for the frequency ranges 100–2000 Hz and 2000–10 000 Hz, respectively. The source is connected to the replica with an adaptation part which features a 2 mm diameter centered communication hole from which the sound radiates inside the vocal tract replica. The acoustic pressure is then measured with a B&K 4182 probe microphone equipped with a 1 mm diameter and a 200 mm long probe. A 3D positioning system (OWIS PS35) allows one to move the probe microphone in all directions with an accuracy of $\pm 1.10^{-4}$ m. However, this accuracy can be reduced by the initial positioning which is less accurate (± 1 mm) and can induce a systematic error. The microphone signal is next transmitted by means of a microphone conditioner (B&K 5935 L) to a data acquisition card (NI PCI-MIO 16 XE) at a sampling frequency of 44 150 Hz. This card is also used to generate the excitation signal which is transmitted to an amplifier (Onkyo a-807) and then to the compression chamber. The whole process is controlled by the LABVIEW program.

The open end of the replica, the microphone, and the positioning system were set inside an insulated room ($1.92 \times 1.95 \times 1.99$ m, Vol $= 7.45\ m^3$, Van Hirtum and Fujiso, 2012). Acoustic foam was placed on the table on which the positioner was located to minimize reflections. The acoustic source was placed outside of the insulated room to avoid interference between the compression chamber and the sound radiated by the replica. A rigid rectangular plane screen made of Plexiglas was set on the exit of the replica to get large dimensions (365×360 mm) compared to the wavelength of interest.

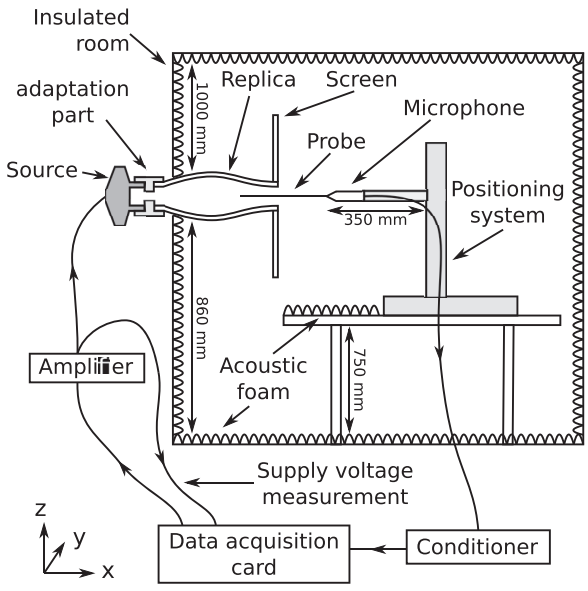

FIG. 4. Experimental setup.

C. Transfer function measurement method

An experimental method has been designed to estimate the transfer function between two points a and b located inside or outside of a waveguide (see Fig. 5).

A sinusoidal signal was generated during 1 s for each frequency. This type of signal allows us to provide enough energy to the replica even when anti-resonance is measured. The acoustic pressure was measured by the probe-microphone at the point a and b. The amplifier output electric signal was recorded synchronously. The amplitude and the phase of the recorded signals were extracted using a Fourier transform of each 1 s recording. This allows one to isolate the frequency component of interest and thus to limit disturbances due to harmonic distortion and noise.

The transfer functions H_{0a} and H_{0b} (see Fig. 5) between the output of the amplifier and the points a and b are first computed. They can be expressed as

$$\begin{cases} H_{0a} = \dfrac{A_a}{A_0} e^{j\phi_{0a}}, \\ H_{0b} = \dfrac{A_b}{A_0} e^{j\phi_{0b}}, \end{cases} \tag{29}$$

where A_a, A_b, A_0, ϕ_{0a}, and ϕ_{0b} are the pressure amplitudes at points a and b, the amplifier output signal amplitude, and the phase differences between the pressures at points a and b and the amplifier output signal.

The transfer function H_{ab} between a and b can then be deduced from H_{0a} and H_{0b} computing the ratio

$$H_{ab} = \frac{H_{0b}}{H_{0a}}. \tag{30}$$

No calibration of the microphone is necessary since the sensitivity factor is eliminated in Eq. (30).

H_{0a} and H_{0b} can be considered as the product of the transfer functions of the amplifier, the source, the acoustic propagation through the replica to the microphone, the

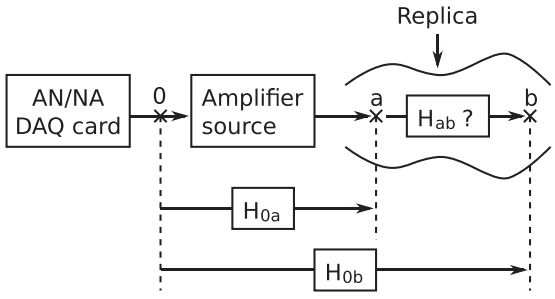

FIG. 5. Transfer function measurement method.

microphone, and the microphone conditioner. These transfer functions are eliminated in Eq. (30) and their influence is thus limited. However, this relies on the assumption that the whole measurement system is linear. This is not the case for the acoustic source, but the effects of the non-linearities are limited by the analysis method which isolates the frequency component of interest, and by the fact that the amplitude of the generated signal is maintained constant during the whole process.

Since they correspond to the ratio of the pressure at two different points and not to the ratio between the pressure at the exit and at the input, the peaks of these transfer functions cannot be considered as formants. However, because of their low sensitivity to experimental artifacts, they are well suited for the comparison with the simulations.

D. Pressure maps

To illustrate the importance of higher order modes and to compare simulations with experiments, the pressure field within the vocal tract and in the near-field was computed and measured at a given frequency for each configuration (see Sec. III A). To do this, the vocal tract was excited at the glottis cross-sectional area with a sinusoidal signal. Its frequency was chosen to coincide with a vocal tract resonance or anti-resonance, which can be obtained from the spectrum of the acoustic pressure at the vocal tract exit. It is thus different from the pressure-pressure transfer function frequencies presented in Tables I and II. Since small differences can be produced between experiments and simulations, these values were extracted for each method to ensure similar pressure distributions. The acoustic pressure was then tracked in a structured grid of points with a distance of 2.5 mm apart (see Fig. 6 for the eccentric /a/). The acoustic pressure amplitude was finally computed to obtain a pressure map.

TABLE I. Resonance frequencies and bandwidths for the pressure-pressure transfer functions in Fig. 6 obtained for two vowel /a/ vocal tract replicas made of two cylindrical tubes with centric and eccentric junctions.

Resonance frequencies (Hz)										
		Plane mode						Higher order modes		
		R1	R2	R3	R4	R5	R6	R7	R8	R9
Centric	Exp	970	2490	3160	4620	5840	8930	—	—	—
	MM	970	2520	3190	4630	5910	9030	—	—	—
	FEM	980	2530	3210	4640	5920	9040	—	—	—
Eccentric	Exp	970	2480	3110	4630	5640	8990	7530	8230	9720
	MM	970	2500	3150	4630	5730	9070	7540	8280	9790
	FEM	980	2510	3160	4650	5740	9040	7480	8240	9720
Resonance bandwidths (Hz)										
Centric	Exp	40	157	159	542	228	422	—	—	—
	MM	31	142	114	482	177	304	—	—	—
	FEM	34	173	153	547	230	386	—	—	—
Eccentric	Exp	45	149	156	[a]	159	316	[a]	195	[a]
	MM	32	132	122	505	117	290	65	169	[a]
	FEM	37	166	160	612	158	353	107	211	[a]

[a]Not measurable.

TABLE II. Resonance and anti-resonance frequencies and bandwidths of examples of transfer functions (presented in Fig. 10) between two points inside of three vowel /a/ vocal tract replicas with centric junctions and circular cross-sections, eccentric junctions and circular cross-sections and eccentric junctions and elliptical cross-sections.

Resonance and anti-resonance frequencies (Hz)							
		Plane mode		Higher order modes		Anti-resonances	
		R1	R2	R3	R4	A1	A2
Centric	Exp	3430	5180	—	—	—	—
	MM	3500	5230	—	—	—	—
	FEM	3450	5210	—	—	—	—
Eccentric	Exp	3360	4970	6600	8320	5790	9530
	MM	3440	5010	6620	8460	5850	9610
	FEM	3410	5020	650	8340	5810	9510
Elliptic	Exp	3340	5120	6730	8550	6300	9790
	MM	3480	5140	6770	8610	6320	9890
	FEM	3440	5140	6730	8510	6290	9790
Resonance and anti-resonance bandwidths (Hz)							
Centric	Exp	227	552	—	—	—	—
	MM	208	512	—	—	—	—
	FEM	213	507	—	—	—	—
Eccentric	Exp	210	478	31	14	30	65
	MM	190	435	14	49	211	102
	FEM	183	446	27	55	72	86
Elliptic	Exp	154	433	54	113	15	72
	MM	184	433	4	17	258	6
	FEM	205	454	41	48	64	8

E. Finite element simulations

The finite element method (FEM) was used to solve the time domain wave equation for the acoustic pressure. First, each one of the vocal tract models presented in Sec. III A were set in a rigid baffle with dimensions $0.3\,\text{m} \times 0.3\,\text{m}$. This baffle constitutes one side of a rectangular volume of $0.3\,\text{m} \times 0.3\,\text{m} \times 0.2\,\text{m}$ in size which allowed sound waves to radiate out from the vocal tract. Free-field radiation conditions were then emulated by means of a perfectly matched layer (PML) of width 0.1 m that surrounded this radiation space and absorbed the outgoing sound waves. The PML was configured to get a reflection coefficient of $r_\infty = 10^{-4}$ at its outer boundary. The resulting computational domains were then meshed using tetrahedral elements with a size that ranged from 0.002 m within the vocal tract and immediate

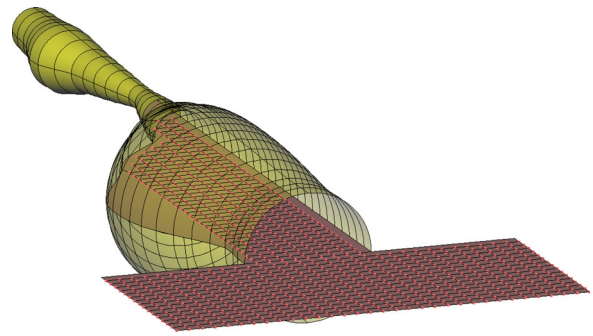

FIG. 6. (Color online) Grid of points for the eccentric /a/, where the acoustic pressure is extracted to compute a pressure map.

outer space, to 0.005 m in the radiation space and 0.0075 m in the PML region.

As far as boundary conditions are concerned, a Gaussian pulse of the type (Arnela and Guasch, 2013)

$$\mathrm{GP}(n) = e^{[(\Delta t\ n - T_{\mathrm{GP}})0.29T_{\mathrm{GP}}]^2}[\mathrm{m}^3/\mathrm{s}], \tag{31}$$

with $T_{\mathrm{GP}} = 0.646/f_0$ and $f_0 = 10$ kHz, was imposed at the vocal tract entrance to compute transfer functions, while a sinusoidal signal, i.e., $\sin(2\pi ft)$, with f corresponding to the frequency of interest was used for obtaining pressure maps (see Sec. III D). To avoid numerical errors beyond the maximum frequency of interest ($f_{\max} = 10$ kHz), the Gaussian pulse was filtered using a low-pass filter with cutoff frequency 10 kHz. At the vocal tract walls, a constant frequency boundary admittance coefficient of $\mu = 0.0025$ was imposed to introduce losses. This value was deemed appropriate after a tuning process, where the resonance bandwidths obtained from simulations were adjusted to fit those from experiments. The baffle where the vocal tracts were set was considered rigid, i.e., $\mu = 0$ on its surface.

A finite element simulation lasting 25 ms for each case was then performed with a sampling rate of $f_s = 1/\Delta t = 2000$ kHz. Such a high frequency rate is needed to fulfill within the meshed computational domains, a stability condition of the Courant–Friedrich–Levy type. A value of $c_0 = 344$ m/s was chosen for the speed of sound, which corresponds to the average temperature value of 21 °C reported during experiments. Details on the finite element formulation and on the derivation of the boundary conditions can be found in Arnela and Guasch (2013) and Arnela *et al.* (2013), respectively.

IV. RESULTS AND DISCUSSION

A. Two cylindrical tubes approximation

The two-tubes geometries are very simple academic cases in which the effect of higher order modes can be highlighted. Indeed, theoretically (Morse and Ingard, 1986) one can predict that the non-planar mode which has the lowest cut-on frequency (6720 Hz at 21 °C) features a nodal line $\psi_n = 0$ located in the middle of the cross-section. ψ_n is positive on one side of this nodal line and negative on the other. In the case of a centric junction both sides of the nodal line are excited by the plane waves coming from the smallest tube. Their contributions to excite this mode compensate each other and is thus zero. In contrast, in the case of an eccentric junction only one side of the nodal line is excited and this mode is expected to be particularly strong inside the larger tube.

1. Transfer functions

Figure 7 presents examples of transfer functions measured and simulated between two points on the longitudinal axis x_3 (see Fig. 1 for x_3 definition). One point is located inside the replica at 30 mm from the source and the other one is outside at 10 mm from the open end. The resonance

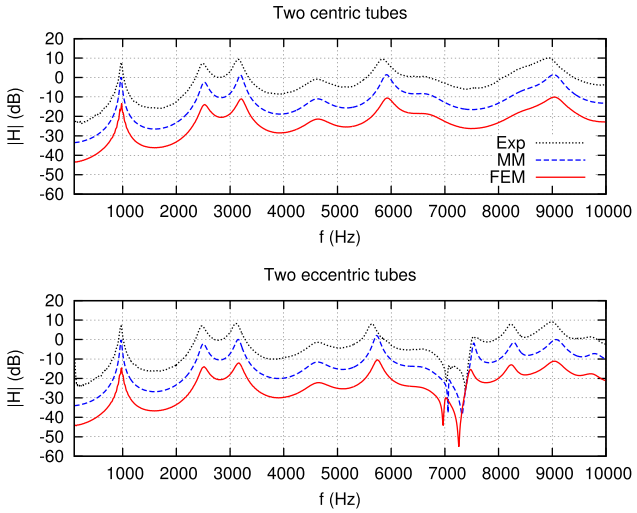

FIG. 7. (Color online) Examples of pressure-pressure transfer functions between two points inside two vowel /a/ vocal tract replicas made of two cylindrical tubes with (top) centric and (bottom) eccentric junctions. The Exp and FEM data have, respectively, been increased and decreased by 10 dB and −10 dB with respect to the MM for visualization purposes. (Exp: experimental data, MM: multimodal method, FEM: finite element method.)

frequencies and their −3 dB bandwidths are listed in Table I.

As expected, in the high frequency range (above 5 kHz) resonances and anti-resonances which are absent in the centric case appear for the eccentric one. In experiments, these anti-resonances are located at 7030 and 7380 Hz while additional resonances are found at 7530, 8230, and 9720 Hz (see Table I). The resonance frequencies of the eccentric case slightly differ from the centric configuration (up to 3.4% lower for R5 of the experimental data) and their bandwidths are smaller (up to 30.2% smaller for R5 of the experimental data). The MM and FEM simulations follow the same trend.

Some small differences can also be observed below 5 kHz. The resonances mainly occur at a lower frequency in the eccentric case compared to the centric configuration (up to 1.6% lower for R3 of the experimental data), except for R1 and R4 which have similar values. This shift down in the resonance frequencies could be explained by the fact that the replica behaves as if it is extended by the eccentricity of the junction. Indeed the midline is longer for the eccentric case.

Both MM and FEM resonance frequencies are close to the experiments, within less than 2%. In general, the bandwidths of the simulations are smaller than those obtained experimentally. This can be understood as an effect of visco-thermal losses. Indeed, accounting for visco-thermal losses would reduce the resonance frequencies and increase their bandwidths (Morse and Ingard, 1986). The MM neglects all visco-thermal losses while FEM account partially for them (see Sec. III E) and are thus closer to the experimental values.

2. Pressure maps

In Fig. 8 it is shown as an example the pressure maps for the centric (top) and eccentric configuration (bottom) when the seventh formant is excited, for both experiments

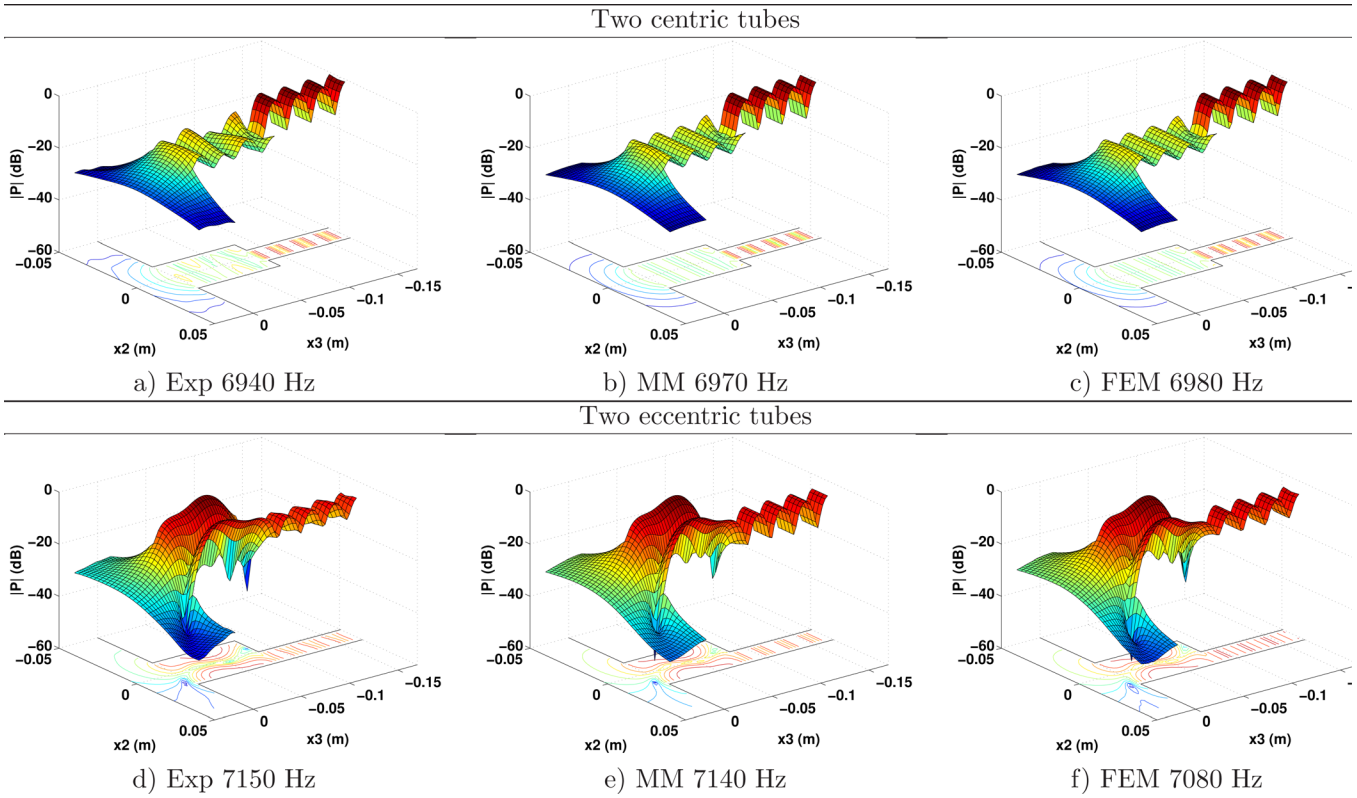

FIG. 8. (Color online) Examples of pressure amplitude maps inside and outside of two vowel /a/ vocal tract replicas made of two cylindrical tubes with a centric (top) and an eccentric (bottom) junction for high frequencies.

and simulations. Some cuts of these pressure maps are also shown in Fig. 9 to compare more easily the measurements and the results obtained with each method.

In agreement with the results observed in the transfer functions, no propagation of the higher order modes can be appreciated on the pressure field in the centric case (see top of Fig. 8). However, the experimental data exhibits some non-planar waveforms [see Fig. 8(a)], in contrast to simulations [see Figs. 8(b) and 8(c)]. Although the greatest care was taken when building the replica, it appears that it is not perfectly symmetrical. As a consequence the first higher order mode is slightly excited and propagates. However, the longitudinal pressure profile along x_3 is located on the nodal line of the first non-planar mode and allows one to observe the effect of the plane mode alone. The measured profile appears to be similar to the one obtained in simulations [see Fig. 9(a)]. Second, the transverse profile along x_2 presented in Fig. 9(b) shows that this effect has a limited impact on the radiated pressure. On the other hand, the iso-amplitude lines are circular outside of the replica [see top of Figs. 8 and 9(b)], showing that the acoustic pressure radiates in spherical waves.

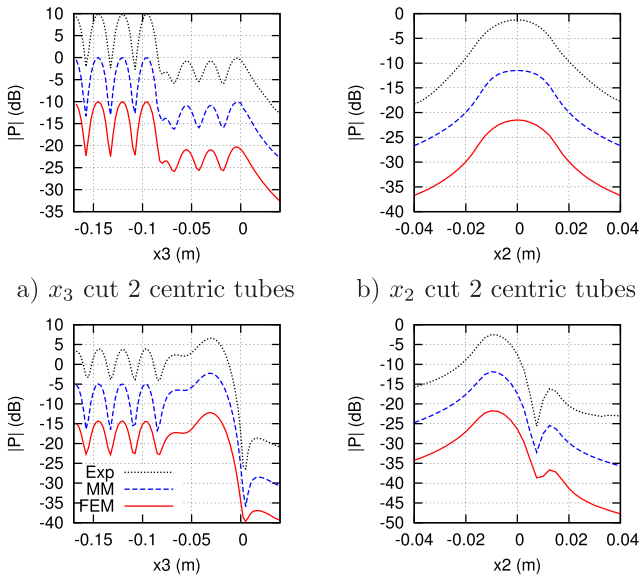

FIG. 9. (Color online) Cuts of the pressure maps in Fig. 8 along the central axis x_3 (left column) and a perpendicular x_2 axis located just in front of the open end (right column) measured and simulated on two vowel /a/ vocal tract replicas made of two cylindrical tubes. A 10 dB shift has been applied between the maxima of the three curves for visualization purposes.

As far as the eccentric case is concerned, the first higher order mode effects can be observed in both experiments and simulations (see bottom of Figs. 8 and 9). While the plane mode is still predominant in the narrowest tube, the first higher order mode becomes predominant in the widest cross-section of the replica. The influence of this mode on the radiated field can be observed as well. The radiated sound pattern is no longer spherical [see bottom of Figs. 8 and 9(d)].

Finally, the different curves shown in Fig. 9 have been quantitatively compared. The mean difference between the experiment and the simulations is less than 1 dB for the centric case and less than 2 dB for the eccentric case.

In summary: The two-tubes replicas point out the evidence for higher order modes in simplified two tubes vocal

geometries. The importance of the connection of the junctions appears to be critical. When present, these higher order modes strongly affect both the internal and the radiated sound field.

B. 44 tubes approximations

In order to study the effect of higher order modes on more realistic geometries, the three vowel /a/ vocal tract replicas presented in Sec. III A have been used. In this case the analysis has been limited to the mid-high frequency range (2–10 kHz), of more interest for the purposes of this work.

1. Transfer functions

Transfer functions between two points inside the replicas located at 80 and 130 mm from the source on x_3 are presented in Fig. 10. The resonances and anti-resonances frequencies and −3 dB bandwidths of these transfer functions have been listed in Table II.

As expected from Sec. IV A, one can observe resonances (R3 and R4) and anti-resonances (A1 and A2) for the geometries which feature eccentric junctions which are not observed for the centric configuration.

In the mid-frequency range (2–5.5 kHz) the resonances occur at lower frequencies for the geometries with eccentric junctions. Indeed, for the experimental data they are up to 4% lower (for R2) for the eccentric and the elliptic /a/.

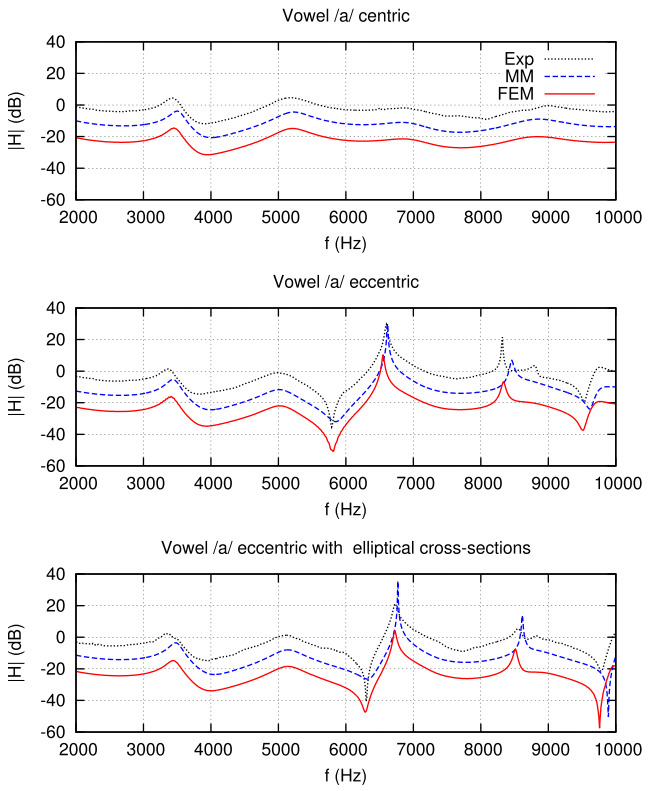

FIG. 10. (Color online) Examples of pressure-pressure transfer functions between two points inside three simplified vowel /a/ vocal tract replicas with (top) centric junctions and circular cross-sections, (middle) eccentric junctions and circular cross-sections and (bottom) eccentric junctions and elliptical cross-sections.

Another effect of the eccentricity at the mid-frequencies is the reduction of the resonance bandwidths. This effect is more important for the elliptic /a/. Thus it appears that the effect of junction eccentricity and cross-section shape on the resonances bandwidths is not negligible even at mid-frequencies.

The transfer function obtained for the elliptic /a/ is similar to the one obtained for the eccentric /a/ up to the high frequencies where the resonance and anti-resonance frequencies are increased for the elliptic /a/ (see middle and bottom of Fig. 10). Indeed, for the elliptic /a/ the frequency of R4 and A1 are, respectively, 230 and 510 Hz higher (or 2.8% and 8.8% higher). These resonance and anti-resonance shifts are in fact produced by the change of cross-sectional shape. From a theoretical point of view, this can be attributed to the propagation modes ψ_n in Eq. (1), which are different for circular and elliptical cross-sections. The cut-on frequency of the propagation mode involved in the appearance of the additional resonances and anti-resonances is increased for the elliptic /a/.

Both MM and FEM simulations are in good agreement with the experiments. The maximal difference between resonances and anti-resonances frequencies is less than 5%. The bandwidths of the simulations are smaller than in the experiments. The difference is more pronounced for the MM. As for the two-tubes replicas this can be attributed to the visco-thermal losses which are partially taken into account by the FEM (see Sec. III E) but neglected by the MM. On the other hand, in the experimental data of Fig. 10 one can notice an additional resonance after R4 for the eccentric and elliptic /a/ which does not appear in the simulations. The presence of this resonance may be due to experimental issues such as positioning error or small imperfections in the replica.

2. Pressure maps

In Fig. 11, examples of pressure maps are presented for the centric /a/ (top), eccentric /a/ (mid), and elliptic /a/ (bottom) at high frequency values for both experiments and simulations. Longitudinal and transversal cuts of these maps along x_3 and x_2 just in front of the open end are provided in Fig. 12.

For the centric /a/, one can observe the effect of the higher order modes inside the replica for the experimental data [see Fig. 11(a)]. This is not the case for the simulated data on which the iso-amplitude lines are perpendicular to x_3 inside the replicas [see Figs. 11(b) and 11(c)]. As for the two-tubes this is probably due to small imperfections of the replica. The pressure profile along the central axis x_3 provided in Fig. 12(a) allows one to observe the effect of the plane mode alone. It appears to be similar to the simulation profiles. On the other hand, the transverse pressure profile along x_2 presented in Fig. 12(b) shows that the effect on the radiated pressure is limited. As a matter of fact, the radiated pressure is spherical.

As expected, this is not the case for the eccentric and elliptic /a/. The effect of the higher order modes inside these replicas can be clearly observed (see middle and

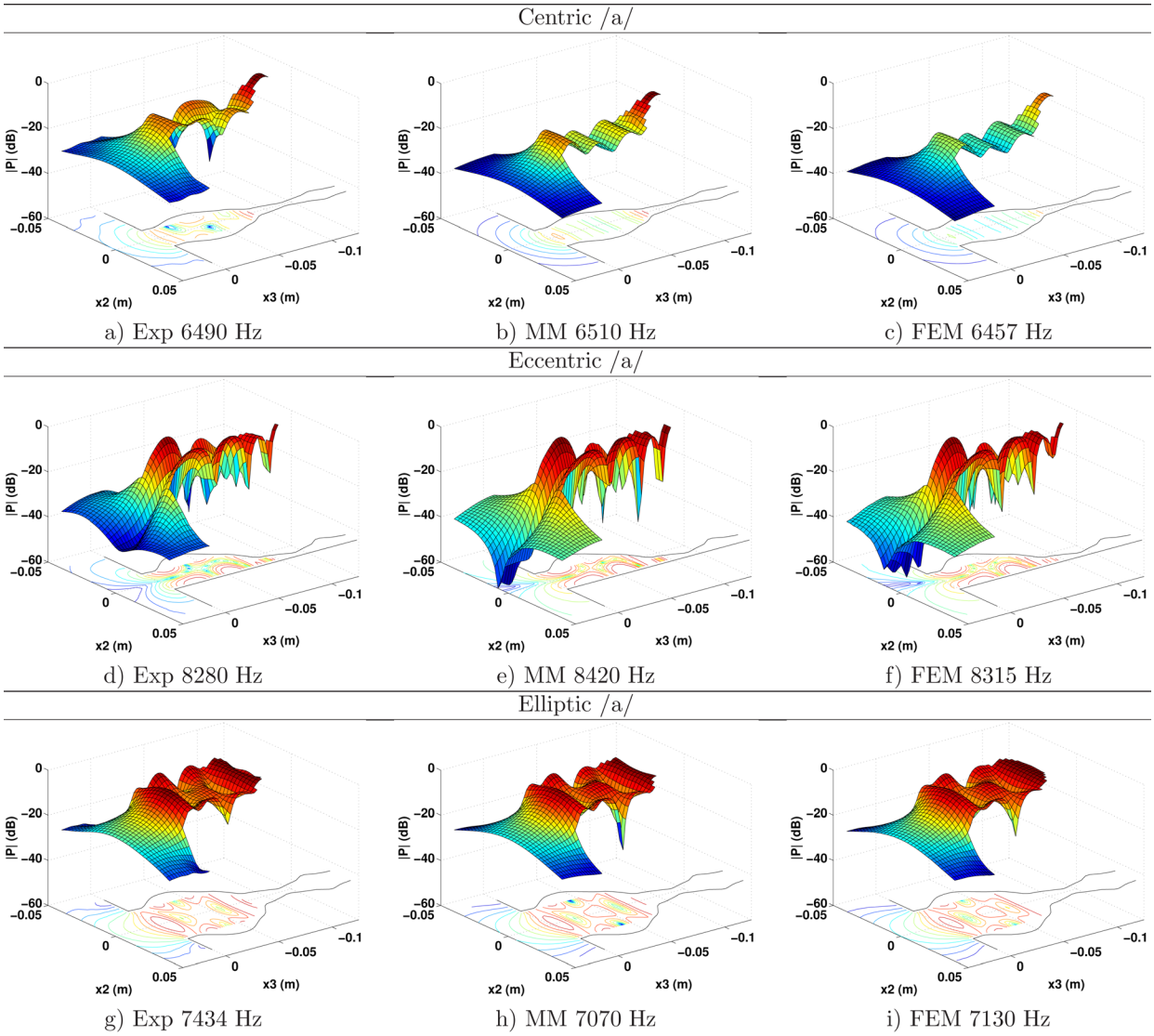

FIG. 11. (Color online) Examples of pressure amplitude maps for high frequencies inside and outside of three simplified vowel /a/ vocal tract replicas with (top) centric junctions and circular cross-sections, (middle) eccentric junctions and circular cross-sections and (bottom) eccentric junctions and elliptical cross-sections.

bottom of Fig. 11). There are local maxima and minima which corresponds to cavity modes. The minima obtained with MM and FEM are more pronounced than those measured experimentally, and the minima of the MM simulations are more important than those of the FEM simulation (see middle and bottom of Figs. 11 and 12). This can be linked with the observations made on the transfer functions: the resonances of the simulations have higher amplitudes and narrower bandwidths. The origin of this difference is probably also the problem of taking visco-thermal losses into account.

The pressure radiated by the eccentric and the elliptic /a/ appears as strongly directional though it is less noticeable for the elliptic /a/ (see middle and bottom of Fig. 11).

In Fig. 12, both MM and FEM simulations show pressure profiles which are close to the experimental data. There are, however, some small differences in the amplitude of the minima and the symmetry of the patterns in the cuts performed along x_2 outside of the vocal tracts [see Figs. 12(b), 12(d), and 12(f)]. In Figs. 12(b) and 12(f), the experimental pressure profile is not perfectly symmetrical, whereas the simulation pressure profiles are. In Fig. 12(d), the two lobes of the experimental data have almost the same amplitude, whereas for both MM and FEM the left lobe has a smaller amplitude than the right lobe. Small differences in the amplitude of the minima can also be observed on the cuts performed along x_3 [see Figs. 12(a), 12(c), and 12(e)]. It is assumed that the difference comes from an experimental artifact due either to some imperfections of the replicas or to reflections on the table which has been insufficiently damped by the acoustic foam.

To compare the cuts of Fig. 12 more directly, the same procedure as for the two-tubes replicas has been followed. The maximal mean difference between the simulations and the experiments is 2.8 dB for the FEM and 2.2 dB for the MM.

In summary: The three configurations for the vowel /a/ highlight the importance of taking higher order modes into

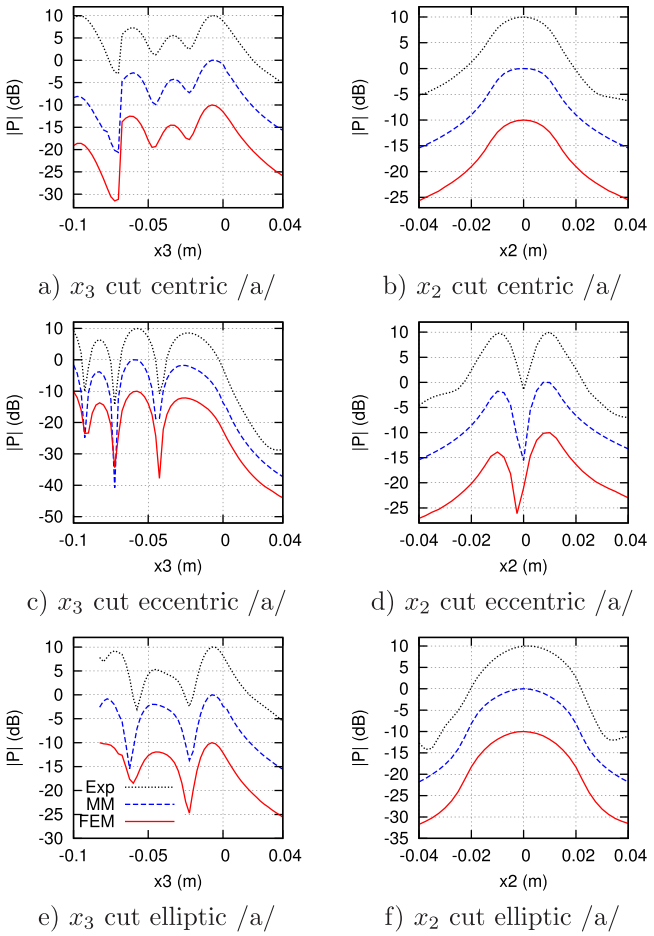

a) x_3 cut centric /a/ b) x_2 cut centric /a/

c) x_3 cut eccentric /a/ d) x_2 cut eccentric /a/

e) x_3 cut elliptic /a/ f) x_2 cut elliptic /a/

FIG. 12. (Color online) Cuts of the pressure maps in Fig. 11 along the propagation axis x_3 (left column) and the axis x_2 just in front of the open end (right column) measured and simulated on three simplified vowel /a/ vocal tract replicas with (top) centric junctions and circular cross-sections, (middle) eccentric junctions and circular cross-sections and (bottom) eccentric junctions and elliptical cross-sections. A 10 dB shift has been applied between the maxima of the three curves for visualization purposes.

account for high frequency simulations of the vocal tract acoustics. The effect of higher order modes on transfer functions and radiation patterns is emphasized by the eccentric and the elliptic /a/ configurations. The measurements and the simulations have also shown that the higher order modes can affect the mid frequency behavior of vocal tract like geometries.

V. CONCLUSION

The conclusions that can be drawn from this study are the following:

(1) Higher acoustical modes can be efficiently predicted using a modal approach. Typical accuracy for resonance frequency is 5%. The resonance bandwidths appeared to be underestimated. This is probably because the visco-thermal losses are neglected in the MM implementation and difficult to take into account with time domain FEM solutions. These losses could be included in the future following Bruneau *et al.* (1987) and Bruneau *et al.* (1989). It is to be noted that some works have already dealt with this loss mechanism using FEM in the frequency domain (see, e.g., Lefebvre and Scavone, 2010). However, the implementation of frequency dependent boundary conditions to consider visco-thermal losses is not a straightforward task in time domain FEM. Some efficient steps towards this goal can be found in Van den Nieuwenhof and Coyette (2001).

(2) At low and mid frequencies (0–5.5 kHz) the higher order modes only slightly change the resonance frequencies and bandwidths. Their effect at high frequency (above 5 kHz) is more spectacular since they generate additional resonances which cannot be predicted using plane wave theory and anti-resonances corresponding to a standing wave perpendicular to the propagation direction.

(3) The higher order modes are highly dependent on the geometrical approximation of the vocal tract. For a given area the cut-on frequency of higher acoustical modes depends on the cross section shape.

(4) The connection between the different sections of the vocal tract approximation is also of great importance. It has been shown that, because of the asymmetry of the first non-planar propagation mode, a centered concatenation of tubes will prevent the apparition of this mode.

(5) The FEM allows studying any complex geometry with any kind of open end but requires a long simulation duration (about 24 h in a serial computing system with processor Intel® Core™ i5 2.8 Ghz for the simulations presented in this paper) and it needs to mesh a part of the outer space. On the other hand, the MM has shorter simulation durations (about 1 h on a desktop computer with processor Intel® Core™ vPro™ 3.0 Ghz for the simulations presented in this paper) and do not require any other discretization than the vocal tract but is limited to simple straight geometries at the present time.

(6) In this work the human head geometry has been roughly approximated by a rigid flat baffle. The effects of more realistic finite flange assumptions (see, e.g., Arnela *et al.*, 2013) on higher order mode propagation will be investigated in the future.

These conclusions indicate that the greatest care should be taken when processing data obtained from imaging techniques such as MRI into 3D geometrical data. The perceptual relevance of these higher acoustical modes can be questioned in the case of vowels since the sound source, the glottal pulses, is essentially of low frequency nature. However, harmonic energy at high frequencies is an essential feature of normal/bright voice quality. Furthermore, the occurrence of higher order acoustical modes is predicted to happen in the range of 4–5 kHz, which corresponds to the maximum of sensitivity of the human ear.

Concerning the radiated sound field, the presence of higher order modes is a plausible explanation for directivity effects at high frequency (Monson *et al.*, 2012) which cannot be explained by plane wave theory. The present study will be extended to the case of fricative sounds for which, due to the wide-band spectrum of the turbulent source as well as its location, higher order modes are expected not only to be essential in terms of propagation and radiation, but also in terms of aeroacoustic interaction with the sound generation (Hirschberg *et al.*, 1995).

ACKNOWLEDGMENTS

This research was supported by EU-FET Grant No. EUNISON 308874. M.A. would like to acknowledge the Generalitat de Catalunya (SUR/ECO) for the predoctoral FI Grant No. 2014FI B2 00142.

Abramowitz, M., and Stegun, I. (**1972**). *Handbook of Mathematical Functions* (Dover, New York), Vol. 1, Chap. 20.

Arnela, M., and Guasch, O. (**2013**). "Finite element computation of elliptical vocal tract impedances using the two-microphone transfer function method," J. Acoust. Soc. Am. **133**, 4197–4209.

Arnela, M., Guasch, O., and Alías, F. (**2013**). "Effects of head geometry simplifications on acoustic radiation of vowel sounds based on time-domain finite-element simulations," J. Acoust. Soc. Am. **134**, 2946–2954.

Bruneau, A., Bruneau, M., Herzog, P., and Kergomard, J. (**1987**). "Boundary layer attenuation of higher order modes in waveguides," J. Sound Vib. **119**, 15–27.

Bruneau, M., Herzog, P., Kergomard, J., and Polack, J. (**1989**). "General formulation of the dispersion equation in bounded visco-thermal fluid, and application to some simple geometries," Wave Motion **11**, 441–451.

Dang, J., and Honda, K. (**1997**). "Acoustic characteristics of the piriform fossa in models and humans," J. Acoust. Soc. Am. **101**, 456–465.

El-Masri, S., Pelorson, X., Saguet, P., and Badin, P. (**1998**). "Development of the transmission line matrix method in acoustics applications to higher modes in the vocal tract and other complex ducts," Int. J. Numer. Model. El. **11**, 133–151.

Fant, G. (**1971**). *Acoustic Theory of Speech Production: With Calculations Based on X-ray Studies of Russian Articulations* (Walter de Gruyter, The Hague), Vol. 2, Chap. 1.

Flanagan, J. L. (**1972**). *Speech Analysis: Synthesis and Perception* (Springer-Verlag, Berlin), Chap. 3.

Fromkin, V. (**1964**). "Lip positions in American English vowels," Lang. Speech **7**, 215–225.

Hirschberg, A., Kergomard, J., and Weinreich, G. (**1995**). *Aero-acoustics of Wind Instruments, Mechanics of Musical Instruments, Lectures Notes CISM* (Springer-Verlag, Wien), pp. 291–369.

Jackson, P., and Shadle, C. (**2000**). "Aero-acoustic modelling of voiced and unvoiced fricatives based on MRI data," in *Proceedings of 5th Speech Production Seminar*, Kloster Seeon, Germany, pp. 185–188.

Kemp, J. (**2002**). "Theoretical and experimental study of wave propagation in brass musical instruments," Ph.D. thesis, University of Edinburgh.

Kemp, J., Campbell, D., and Amir, N. (**2001**). "Multimodal radiation impedance of a rectangular duct terminated in an infinite baffle," Acta Acust. Acust. **87**, 11–15.

Kergomard, J., Garcia, A., Tagui, G., and Dalmont, J. (**1989**). "Analysis of higher order mode effects in an expansion chamber using modal theory and equivalent electrical circuits," J. Sound Vib. **129**, 457–475.

Kniesburges, S. (**2013**). "Influence of vortical flow structures on the glottal jet location in the supraglottal region," J. Voice **27**, 531–544.

Lefebvre, A., and Scavone, G. (**2010**). "Finite element modeling of woodwind instruments," in *Proceedings of ISMA*.

Monson, B., Hunter, E., and Story, B. (**2012**). "Horizontal directivity of low- and high-frequency energy in speech and singing," J. Acoust. Soc. Am. **132**, 433–441.

Morse, P., and Ingard, K. (**1986**). *Theoretical Acoustics* (Princeton University Press, Princeton), Chap. 9.

Motoki, K., Badin, P., Pelorson, X., and Matsuzaki, H. (**2000**). "A modal parametric method for computing acoustic characteristics of three-dimensional vocal tract models," in *Proceedings of the 5th Seminar on Speech Production: Models and Data*, pp. 325–328.

Motoki, K., Miki, N., and Nagai, N. (**1992**). "Measurement of sound-pressure distribution in replicas of the oral cavity," J. Acoust. Soc. Am. **92**, 2577–2585.

Narayanan, S., Alwan, A., and Haker, K. (**1995**). "An articulatory study of fricative consonants using magnetic resonance imaging," J. Acoust. Soc. Am. **98**, 1325–1347.

O'Shaughnessy, D. (**1987**). *Speech Communication: Human and Machine, Addison-Wesley Series in Electrical Engineering: Digital Signal Processing* (Wiley-IEEE Press, Piscataway, NJ), Chap. 3.

Pagneux, V., Amir, N., and Kergomard, J. (**1996**). "A study of wave propagation in varying cross-section waveguides by modal decomposition. Part I. Theory and validation," J. Acoust. Soc. Am. **100**, 2034–2048.

Roure, A. (**1976**). "Propagation guidée. etude des discontinuités" ("Guided propagation. Study of discontinuities"), Ph.D. thesis, Université d'Aix-Marseille, Marseille.

Stevens, K. (**2000**). *Acoustic Phonetics* (MIT Press, Cambridge, MA), Vol. 30, Chap. 3.

Story, B. (**2008**). "Comparison of magnetic resonance imaging-based vocal tract area functions obtained from the same speaker in 1994 and 2002," J. Acoust. Soc. Am. **123**, 327–335.

Takemoto, H., Mokhtari, P., and Kitamura, T. (**2010**). "Acoustic analysis of the vocal tract during vowel production by finite-difference time-domain method," J. Acoust. Soc. Am. **128**, 3724–3738.

Thomson, S., Mongeau, L., and Frankel, S. (**2005**). "Aerodynamic transfer of energy to the vocal folds," J. Acoust. Soc. Am. **118**, 1689–1700.

Vampola, T., Horácek, J., Laukkanen, A.-M., and Švec, J. G. (**2013**). "Human vocal tract resonances and the corresponding mode shapes investigated by three-dimensional finite-element modelling based on CT measurement," Logoped. Phoniat. Vocol., doi:10.3109/14015439.2013.775333, 1–10.

Van den Nieuwenhof, B., and Coyette, J. (**2001**). "Treatment of frequency-dependent admittance boundary conditions in transient acoustic finite/infinite-element models," J. Acoust. Soc. Am. **110**, 1743–1751.

Van Hirtum, A., and Fujiso, Y. (**2012**). "Insulation room for aero-acoustic experiments at moderate Reynolds and low Mach numbers," Appl. Acoust. **73**, 72–77.

Woo, J., Murano, E., Stone, M., and Prince, J. (**2012**). "Reconstruction of high-resolution tongue volumes from MRI," IEEE Trans. Biomed. Eng. **59**, 3511–3524.

Zheng, X., Mittal, R., Xue, Q., and Bielamowicz, S. (**2011**). "Direct-numerical simulation of the glottal jet and vocal-fold dynamics in a three-dimensional laryngeal model," J. Acoust. Soc. Am. **130**, 404–415.

Zorumski, W. (**1973**). "Generalized radiation impedances and reflection coefficients of circular and annular ducts," J. Acoust. Soc. Am. **54**, 1667–1673.